

Title: Structure-based Design of Prefusion-stabilized SARS-CoV-2 Spikes

Authors: Ching-Lin Hsieh¹, Jory A. Goldsmith¹, Jeffrey M. Schaub¹, Andrea M. DiVenere², Hung-Che Kuo¹, Kamyab Javanmardi¹, Kevin C. Le², Daniel Wrapp¹, Alison Gene-Wei Lee¹, Yutong Liu², Chia-Wei Chou¹, Patrick O. Byrne¹, Christy K. Hjorth¹, Nicole V. Johnson¹, John Ludes-Meyers¹, Annalee W. Nguyen², Juyeon Park¹, Nianshuang Wang¹, Dzifa Amengor¹, Jennifer A. Maynard^{2*}, Ilya J. Finkelstein^{1,3*}, Jason S. McLellan^{1*}

Affiliations:

¹ Department of Molecular Biosciences, The University of Texas at Austin, Austin, Texas 78712

²Department of Chemical Engineering, University of Texas at Austin, Austin, Texas 78712

³Center for Systems and Synthetic Biology, University of Texas at Austin, Austin, Texas 78712

*Correspondence: maynard@che.utexas.edu, ilya@finkelsteinlab.org,

jmclellan@austin.utexas.edu

1 **ABSTRACT**

2 The COVID-19 pandemic caused by the novel coronavirus SARS-CoV-2 has led to accelerated
3 efforts to develop therapeutics, diagnostics, and vaccines to mitigate this public health
4 emergency. A key target of these efforts is the spike (S) protein, a large trimeric class I fusion
5 protein that is metastable and difficult to produce recombinantly in large quantities. Here, we
6 designed and expressed over 100 structure-guided spike variants based upon a previously
7 determined cryo-EM structure of the prefusion SARS-CoV-2 spike. Biochemical, biophysical
8 and structural characterization of these variants identified numerous individual substitutions that
9 increased protein yields and stability. The best variant, HexaPro, has six beneficial proline
10 substitutions leading to ~10-fold higher expression than its parental construct and is able to
11 withstand heat stress, storage at room temperature, and multiple freeze-thaws. A 3.2 Å-resolution
12 cryo-EM structure of HexaPro confirmed that it retains the prefusion spike conformation. High-
13 yield production of a stabilized prefusion spike protein will accelerate the development of
14 vaccines and serological diagnostics for SARS-CoV-2.

15 INTRODUCTION

16 Coronaviruses are enveloped viruses containing positive-sense RNA genomes. Four human
17 coronaviruses generally cause mild respiratory illness and circulate annually. However, SARS-
18 CoV and MERS-CoV were acquired by humans via zoonotic transmission and caused outbreaks
19 of severe respiratory infections with high case-fatality rates in 2002 and 2012, respectively^{1,2}.
20 SARS-CoV-2 is a novel betacoronavirus that emerged in Wuhan, China in December 2019 and
21 is the causative agent of the ongoing COVID-19 pandemic^{3,4}. As of May 26, 2020, the WHO has
22 reported over 5 million cases and 350,000 deaths worldwide. Effective vaccines, therapeutic
23 antibodies and small-molecule inhibitors are urgently needed, and the development of these
24 interventions is proceeding rapidly.

25 Coronavirus virions are decorated with a spike (S) glycoprotein that binds to host-cell
26 receptors and mediates cell entry via fusion of the host and viral membranes⁵. S proteins are
27 trimeric class I fusion proteins that are expressed as a single polypeptide that is subsequently
28 cleaved into S1 and S2 subunits by cellular proteases^{6,7}. The S1 subunit contains the receptor-
29 binding domain (RBD), which, in the case of SARS-CoV-2, recognizes the angiotensin-
30 converting enzyme 2 (ACE2) receptor on the host-cell surface^{8–10}. The S2 subunit mediates
31 membrane fusion and contains an additional protease cleavage site, referred to as S2', that is
32 adjacent to a hydrophobic fusion peptide. Binding of the RBD to ACE2 triggers S1 dissociation,
33 allowing for a large rearrangement of S2 as it transitions from a metastable prefusion
34 conformation to a highly stable postfusion conformation^{6,11}. During this rearrangement, the
35 fusion peptide is inserted into the host-cell membrane after cleavage at S2', and two heptad
36 repeats in each protomer associate to form a six-helix bundle that brings together the N- and C-
37 termini of the S2 subunits as well as the viral and host-cell membranes. Attachment and entry are

38 essential for the viral life cycle, making the S protein a primary target of neutralizing antibodies
39 and a critical vaccine antigen^{12,13}.

40 A stabilized prefusion conformation of class I fusion proteins is desirable for vaccine
41 development because this conformation is found on infectious virions and displays most or all of
42 the neutralizing epitopes that can be targeted by antibodies to prevent the entry process^{14–16}. We
43 and others have observed that prefusion stabilization tends to increase the recombinant
44 expression of viral glycoproteins, possibly by preventing triggering or misfolding that results
45 from a tendency to adopt the more stable postfusion structure. For example, structure-based
46 design of prefusion-stabilized MERS-CoV and SARS-CoV spike ectodomains resulted in
47 homogeneous preparations of prefusion spikes and greatly increased yields¹⁵. These variants (S-
48 2P) contained two consecutive proline substitutions in the S2 subunit in a turn between the
49 central helix (CH) and heptad repeat 1 (HR1) that must transition to a single, elongated α -helix in
50 the postfusion conformation. Prefusion-stabilized spike variants are also superior immunogens to
51 wild-type spike ectodomains¹⁵, and have been used to determine high-resolution spike structures
52 by cryo-EM^{17–20}. Importantly, the successful transplantation of this double-proline substitution
53 into the SARS-CoV-2 spike (SARS-CoV-2 S-2P) allowed for the rapid determination of high-
54 resolution cryo-EM structures and accelerated development of vaccine candidates^{21,22}. However,
55 even with these substitutions, the SARS-CoV-2 S-2P ectodomain is unstable and difficult to
56 produce reliably in mammalian cells, hampering biochemical research and development of
57 subunit vaccines.

58 Here, we employ structure-based design to increase the yield and stability of the SARS-
59 CoV-2 spike ectodomain in the prefusion conformation. We report multiple prolines, disulfide
60 bonds, salt bridges, and cavity-filling substitutions that increase expression and/or stability of the

61 spike relative to the S-2P base construct. Combining four proline substitutions into a single
62 construct, termed HexaPro, stabilized the prefusion state and increased expression 10-fold. A
63 high-resolution cryo-EM structure of this variant confirms that the proline substitutions adopt the
64 designed conformations and do not disrupt the conformation of the S2 subunit, thus preserving
65 its antigenicity. This work will facilitate production of prefusion spikes for diagnostic kits and
66 subunit vaccines, and has broad implications for next-generation coronavirus vaccine design.

67 **RESULTS**

68 **Structure-based design of prefusion-stabilized SARS-CoV-2 spikes**

69 To generate a prefusion-stabilized SARS-CoV-2 spike protein that expresses at higher levels and
70 is more stable than our original S-2P construct²¹ we analyzed the SARS-CoV-2 S-2P cryo-EM
71 structure (PDB ID: 6VSB) and designed substitutions based upon knowledge of class I fusion
72 protein function and general protein stability principles. These strategies included the
73 introduction of disulfide bonds to prevent conformational changes during the pre-to-postfusion
74 transition, salt bridges to neutralize charge imbalances, hydrophobic residues to fill internal
75 cavities, and prolines to cap helices or stabilize loops in the prefusion state. We cloned 100
76 single S-2P variants and characterized their relative expression levels (**Table S1**), and for those
77 that expressed well we characterized their monodispersity, thermostability, and quaternary
78 structure. Given that the S2 subunit undergoes large-scale refolding during the pre-to-postfusion
79 transition, we exclusively focused our efforts on stabilizing S2. Substitutions of each category
80 were identified that increased expression while maintaining the prefusion conformation (**Fig. 1**
81 **and 2A**). Overall, 26 out of the 100 single-substitution variants had higher expression than S-2P
82 (**Table S1**).

83 **Single-substitution spike variants**

84 One common strategy to stabilize class I fusion proteins, such as the spike, is to covalently link a
85 region that undergoes a conformational change to a region that does not via a disulfide bond. For
86 instance, the Q965C/S1003C substitution attempts to link HR1 to the central helix, whereas
87 G799C/A924C aims to link HR1 to the upstream helix. These two variants boosted protein
88 expression 3.8-fold and 1.3-fold compared to S-2P, respectively (**Fig. 2B**). However, the size-
89 exclusion chromatography (SEC) traces of both variants showed a leftward shift compared to S-
90 2P, indicating that the proteins were running larger than expected, which agreed well with
91 negative stain electron microscopy (nsEM) results that showed partially misfolded spike particles
92 (**Fig. S1**). In contrast, S884C/A893C and T791C/A879C variants eluted on SEC at a volume
93 similar to S-2P and were well-folded trimeric particles by nsEM (**Fig. 2E**). These variants link
94 the same α -helix to two different flexible loops that pack against a neighboring protomer (**Fig.**
95 **1**). Notably, S884C/A893C had two-fold higher expression than S-2P with increased
96 thermostability (**Fig. 2F**).

97 Cavity-filling substitutions and salt bridges can also enhance protein stability without
98 disturbing the overall fold. Cavity filling has been particularly helpful in stabilizing the prefusion
99 conformations of RSV F and HIV-1 Env^{23,24}. We found many cavity-filling and salt bridge
100 designs that improved protein expression compared to S-2P (**Fig. 2G**). For example, L938F and
101 T961D both produced ~2-fold increases in protein yield and maintained the correct quaternary
102 structure (**Fig. 2C and 2E**), although the thermostability of both variants as assessed by
103 differential scanning fluorimetry (DSF) was unchanged compared to S-2P (**Fig. 2F**).

104 Previous successes using proline substitutions inspired us to investigate 14 individual
105 variants wherein a proline was substituted into flexible loops or the N-termini of helices in the
106 fusion peptide, HR1, and the region connecting them (CR) (**Table 1 and Fig. 1G**). As expected,

107 multiple proline variants boosted the protein expression and increased the thermostability (**Fig.**
108 **2D and 2F**). Two of the most successful substitutions, F817P and A942P, exhibited 2.8 and 6.0-
109 fold increases in protein yield relative to S-2P, respectively. The A942P substitution further
110 increased the melting temperature (Tm) by ~3 °C, and both variants appeared as well-folded
111 trimers by nsEM (**Fig. 2E** and **Fig. S2**).

112 **Multi-substitution spike variants**

113 We next generated combination (“Combo”) variants that combined the best-performing
114 modifications from our initial screen. The Combo variants containing two disulfide bonds
115 generally expressed 2-fold lower than the single-disulfide variants, suggesting that they
116 interfered with each other (**Table S2**). Adding one disulfide (S884C/A893C) to a single proline
117 variant (F817P) also reduced the expression level, although the quaternary structure of the spikes
118 was well maintained (**Table S2**, Combo40). The beneficial effect of a disulfide bond was most
119 prominent when combined with L938F, a cavity-filling variant. Combo23 (S884C/A893C,
120 L938F) had higher protein yields than either of its parental variants, but the Tm of Combo23 did
121 not increase compared to S884C/A893C (**Fig. S3B**). In addition, mixing one cavity-filling
122 substitution with one proline substitution (Combo20) increased the expression compared to
123 L938F alone (**Table S2**).

124 Combining multiple proline substitutions resulted in the most drastic increases in
125 expression and stability (**Fig. 3A**). Combo14, containing A892P and A942P, had a 6.2-fold
126 increase in protein yield compared to A892P alone (**Fig. 3B and 3C**). Adding a third proline,
127 A899P, increased thermostability (+1.2 °C Tm) but did not further increase expression (**Fig. 3C**).
128 Combo46 (A892P, A899P, F817P) had a 3.4-fold increase in protein yield and a 3.3 °C rise in
129 Tm as compared to A892P. The most promising variant, Combo47, renamed HexaPro, contains

130 all four beneficial proline substitutions (F817P, A892P, A899P, A942P) as well as the two
131 proline substitutions in S-2P. HexaPro expressed 9.8-fold higher than S-2P, had ~5 °C increase
132 in Tm, and retained the trimeric prefusion conformation (**Fig. 3D, Fig. S2**). We focused on this
133 construct for additional characterization.

134 **HexaPro large-scale expression and stress testing**

135 To assess the viability of HexaPro as a potential vaccine antigen or diagnostic reagent, we
136 comprehensively examined large-scale production in FreeStyle 293-F cells, the feasibility of
137 protein expression in ExpiCHO cells, epitope integrity and protein stability. We were able to
138 generate ~14 mg of HexaPro from 2L of FreeStyle 293-F cells, or 7 mg/L, which represents a
139 greater than 10-fold improvement over S-2P²¹. Importantly, large-scale HexaPro preparations
140 retained a monodisperse SEC peak corresponding to the molecular weight of a glycosylated
141 trimer (**Fig. 4A**) and were indistinguishable from S-2P by nsEM (**Fig. 4B**). Industrial production
142 of recombinant proteins typically relies on CHO cells rather than HEK293 cells. We thus
143 investigated HexaPro expression in ExpiCHO cells via transient transfection. ExpiCHO cells
144 produced 1.3 mg of well-folded protein per 40 mL of culture, or 32.5 mg/L (**Fig. 4C and 4D**).
145 The binding kinetics of HexaPro to the human ACE2 receptor were comparable to that of S-2P
146 (**Fig. 4E and 4F**), with affinities of 13.3 nM and 11.3 nM, respectively. HexaPro remained
147 folded in the prefusion conformation after 3 cycles of freeze-thaw, 2 days incubation at room
148 temperature or 30 minutes at 55 °C (**Fig. 4G and 4H**). In contrast, S-2P showed signs of
149 aggregation after 3 cycles of freeze-thaw, and began unfolding after 30 min at 50 °C.
150 Collectively, these data indicate that HexaPro is a promising candidate for SARS-CoV-2 vaccine
151 development.

152 **Cryo-EM structure of SARS-CoV-2 S HexaPro**

153 To confirm that our stabilizing substitutions did not lead to any unintended conformational
154 changes, we determined the cryo-EM structure of SARS-CoV-2 S HexaPro. From a single
155 dataset, we were able to obtain high-resolution 3D reconstructions for two distinct conformations
156 of S: one with a single RBD in the up conformation and the other with two RBDs in the up
157 conformation. This two-RBD-up conformation was not observed during previous structural
158 characterization of SARS-CoV-2 S-2P^{21,22}. While it is tempting to speculate that the enhanced
159 stability of S2 in HexaPro allowed us to observe this less stable intermediate, validating this
160 hypothesis will require further investigation. Roughly a third (30.6%) of the particles were in the
161 two-RBD-up conformation, leading to a 3.20 Å reconstruction. The remaining particles were
162 captured in the one-RBD-up conformation, although some flexibility in the position of the
163 receptor-accessible RBD prompted us to remove a subset of one-RBD-up particles that lacked
164 clear density for this domain, resulting in a final set of 85,675 particles that led to a 3.21 Å
165 reconstruction (**Fig. 5A**, **Fig. S4** and **Fig. S5**). Comparison of our one-RBD-up HexaPro
166 structure with the previously determined 3.46 Å S-2P structure revealed an RMSD of 1.2 Å over
167 436 Cα atoms in S2 (**Fig. 5B**). The relatively high resolution of this reconstruction allowed us to
168 confirm that the stabilizing proline substitutions did not distort the S2 subunit conformation (**Fig.**
169 **5C**).

170 **DISCUSSION**

171 Prefusion-stabilized class I viral fusion proteins generally induce more potent neutralizing
172 antibodies and function as better vaccine antigens than their unstabilized counterparts^{14–16}. To
173 respond to the urgent need for preventative countermeasures against the COVID-19 pandemic,
174 we used our prefusion-stabilized SARS-CoV-2 S-2P structure²¹ as a guide to design 100 single

175 substitution variants intended to have increased expression or stability. We focused on
176 engineering the S2 subunit because it undergoes large-scale refolding to facilitate membrane
177 fusion. One of the strategies we employed was the introduction of disulfide bonds wherein at
178 least one cysteine is in a region that changes conformation between the pre- and postfusion
179 states. Although this method has been successful in the case of HIV-1 Env (SOSIP) and RSV F
180 (DS-Cav1)^{14,23}, the disulfides we introduced into S2 generally had detrimental effects. For
181 example, inter-subunit disulfides (e.g. S659C/S698C) decreased the protein expression by 60%
182 (**Table S1**), and the Q965C/S1003C substitution led to partially mis-folded spikes (**Fig. 2B**).
183 Inter-protomer disulfides have been shown to improve the trimer integrity of HIV-1 Env and the
184 stability of RSV F^{25,26}, but the inter-protomeric T961C/S758C substitution ablated expression
185 (**Table S1**). In contrast, we found that stabilizing the flexible loops located in the protomer
186 interfaces was beneficial. Both S884C/A893C and T791C/A879C increased thermostability or
187 expression and resulted in native trimer structures. It is possible that anchoring flexible loops to a
188 relatively rigid α -helix favors protomer assembly.

189 Introducing a salt bridge at the HIV-1 gp120–gp41 interface not only boosted the protein
190 expression but also enhanced the binding of trimer-specific antibodies, suggesting improved
191 retention of the native quaternary structure²⁴. Based on a similar principle, the T961D
192 substitution was introduced to form an electrostatic interaction with Arg765 from a neighboring
193 protomer (**Fig. 1**). Likewise, the G769E substitution was designed to form an inter-protomeric
194 salt bridge with Arg1014. Both variants increased expression and resembled well-folded trimers
195 (**Fig. 2E, Fig. S2, Table S1**). In addition to salt bridges, filling loosely packed
196 hydrophobic cores that allow the protein to refold can help stabilize the prefusion state, as shown
197 by previous cavity-filling substitutions in RSV F and HIV-1 Env^{14,23,27}. Here, the L938F

198 substitution was designed to fill a cavity formed in part by HR1, the FP and a β -hairpin (**Fig. 1**).
199 This variant had a 2-fold increase in expression (**Fig. 2C**) and appeared to have additive effects
200 when paired with disulfide or proline substitutions (**Table S2**).

201 Among the best single-substitution variants we discovered were F817P and A942P (**Fig**
202 **2**). By further combining them with A892P and A899P substitutions, we generated the highest
203 expressing construct, HexaPro. This result is reminiscent of previous successful applications of
204 proline substitutions to class I fusion proteins including HIV-1 Env, influenza HA, RSV F,
205 hMPV F, MERS-CoV S, Lassa GPC and Ebola GP^{14,15,23,28–31}. Solvent accessibility of
206 hydrophobic residues near the fusion peptide was a concern for influenza HA stem-only
207 designs³², and similarly we addressed this issue by replacing the exposed Phe817 with Pro (**Fig.**
208 **5C**). The A942P substitution imposes rigidity to the flexible loop between the connector region
209 and HR1, and is similar to that of the T577P substitution found to be helpful for stabilizing Ebola
210 GP²⁸.

211 In our HexaPro cryo-EM dataset we observed a third of the particles in a two-RBD-up
212 conformation. This had not been previously observed for SARS-CoV-2 spikes until a recent
213 structure was determined of a modified spike containing four hydrophobic substitutions that
214 brought subdomain 1 closer to S2³³. We hypothesize that the more stable S2 in HexaPro allowed
215 us to capture this relatively unstable conformation that may transiently exist prior to triggering
216 and dissociation of S1. This is similar to what was observed in the structures of the MERS-CoV
217 S-2P spike, where even the 3-RBD-up conformation could be observed¹⁵. Additionally, HexaPro
218 spikes were able to retain the prefusion state after freeze-thaws, room temperature storage, and
219 heat stress, which should aid in the development of HexaPro spikes as subunit vaccine antigens.
220 HexaPro spikes may also improve DNA or mRNA-based vaccines by producing more antigen

221 per nucleic acid molecule, thus improving efficacy at the same dose or maintaining efficacy at
222 lower doses. Finally, we demonstrate that 32 mg of well-folded HexaPro can be obtained from
223 1L of ExpiCHO cells, indicating a clear path to industrial-level production to meet global
224 demand for this essential SARS-CoV-2 protein.

225 **ACKNOWLEDGMENTS**

226 We thank members of the Maynard, Finkelstein, and McLellan Laboratories for providing
227 helpful comments on the manuscript. In addition, we would like to thank Dr. Thomas Edwards
228 and Ulrich Baxa for cryo-EM data collection. We also thank Dr. Eric Fich for providing helpful
229 data analysis. This work was supported by NIH grant R01-AI127521 to J.S.M., and grants from
230 the Welch Foundation (F-1808 to I.J.F.), the NIH (GM120554 and GM124141 to I.J.F) and the
231 NSF (1453358 to I.J.F.). I.J.F. is a CPRIT Scholar in Cancer Research. This research was, in
232 part, supported by the National Cancer Institute's National Cryo-EM Facility at the Frederick
233 National Laboratory for Cancer Research under contract HSSN261200800001E. The Sauer
234 Structural Biology Laboratory is supported by the University of Texas College of Natural
235 Sciences and by award RR160023 from the Cancer Prevention and Research Institute of Texas
236 (CPRIT).

237 **AUTHOR CONTRIBUTIONS**

238 Conceptualization, C.-L.H. and J.S.M.; Investigation and visualization, C.-L.H., J.A.G., C.-W.C.,
239 A.M.D., K.J., H.-C.K., K.C.L., A.G.-W.L., Y.L., J.M.S., D.W., P.O.B., C.K.H., N.V.J., J.L.-M.,
240 A.W.N., J.P., and D.A.; Writing – Original Draft, C.-L.H., J.A.G., D.W., P.O.B., C.K.H., N.V.J.,
241 and J.S.M; Writing – Reviewing & Editing, C.-L.H., J.A.G., D.W., P.O.B., N.W., C.K.H.,
242 N.V.J., J.A.M., I.J.F., and J.S.M.; Supervision, J.A.M., I.J.F. and J.S.M.

243 **COMPETING INTERESTS**

244 N.W. and J.S.M. are inventors on U.S. patent application no. 62/412,703 (“Prefusion
245 Coronavirus Spike Proteins and Their Use”). D.W., N.W. and J.S.M. are inventors on U.S. patent
246 application no. 62/972,886 (“2019-nCoV Vaccine”). C.-L.H., J.A.G., J.M.S., C.-W.C., A.M.D.,
247 K.J., H.-C.K., D.W., P.O.B., C.K.H., N.V.J., N.W., J.A.M., I.J.F., and J.S.M. are inventors on
248 U.S. patent application no. 63/032,502 (“Engineered Coronavirus Spike (S) Protein and Methods
249 of Use Thereof”).

250 **FIGURE LEGENDS**

251 **Figure 1. Exemplary substitutions for SARS-CoV-2 spike stabilization.** Side view of the
252 trimeric SARS-CoV-2 spike ectodomain in a prefusion conformation (PDB ID: 6VSB). The S1
253 domains are shown as a transparent molecular surface. The S2 domain for each protomer is
254 shown as a ribbon diagram. Each inset corresponds to one of four types of spike modifications
255 (proline, salt bridge, disulfide, cavity filling). Side chains in each inset are shown as red spheres
256 (proline), yellow sticks (disulfide), red and blue sticks (salt bridge) and orange spheres (cavity
257 filling).

258 **Figure 2. Characterization of single-substitution spike variants.** (A) SDS-PAGE of SARS-
259 CoV-2 S-2P and single-substitution spike variants. Molecular weight standards are indicated at
260 the left in kDa. (B-D) Size-exclusion chromatography of purified spike variants, grouped by type
261 (B, disulfide variants; C, cavity filling and salt bridge; D, proline). A vertical dotted line
262 indicates the characteristic peak retention volume for S-2P. (E) Representative negative stain
263 electron micrographs for four variants. (F) Differential scanning fluorimetry analysis of spike
264 variant thermostability. The vertical dotted line indicates the first apparent melting temperature
265 for S-2P. (G) Concentrations of individual variants in culture medium, determined by

266 quantitative biolayer interferometry. Variants are colored by type. The horizontal dotted line
267 indicates the calculated concentration of S-2P, which was used as a control for comparison.

268 **Figure 3. Characterization of multi-substitution spike variants.** (A) SDS-PAGE of SARS-
269 CoV-2 Combo variants. Molecular weight standards are indicated at the left in kDa. (B) SEC
270 traces for S-2P, A892P and four Combo variants. The vertical dotted line indicates the peak
271 retention volume for S-2P. (C) DSF analysis of Combo variant thermostability. The black
272 vertical dotted line indicates the first apparent melting temperature for S-2P, the green vertical
273 dotted line shows the first apparent melting temperature for Combo47 (HexaPro). (D) Negative
274 stain electron micrograph of purified Combo47 (HexaPro).

275 **Figure 4. HexaPro exhibits enhanced expression and stability compared to S-2P.** (A) SEC
276 trace of a portion of the HexaPro purified from a 2L culture of FreeStyle 293-F cells. (B)
277 Negative stain electron micrograph of HexaPro purified from FreeStyle 293-F cells. (C) SEC
278 trace of HexaPro after purification from a 40 ml culture of ExpiCHO cells. (D) Negative stain
279 electron micrograph of HexaPro from ExpiCHO cells. (E-F) Binding of S-2P (E) and HexaPro
280 (F) to human ACE2 assessed by surface plasmon resonance. Binding data are shown as black
281 lines and the best fit to a 1:1 binding model is shown as red lines. (G-H) Assessment of protein
282 stability by negative stain electron microscopy. The top row of micrographs in (G) and (H)
283 corresponds to S-2P, the bottom row corresponds to HexaPro.

284 **Figure 5. High resolution cryo-EM structure of HexaPro.** (A) EM density map of trimeric
285 HexaPro. Each protomer is shown in a different color; the protomer depicted in wheat adopts the
286 RBD-up conformation. (B) Alignment of an RBD-down protomer from HexaPro (green ribbon)
287 with an RBD-down protomer from S-2P (white ribbon, PDB ID: 6VSB). (C) Zoomed view of

288 the four proline substitutions unique to HexaPro. The EM density map is shown as a transparent
289 surface, individual atoms are shown as sticks. Nitrogen atoms are colored blue and oxygen atoms
290 are colored red.

291 **SUPPLEMENTAL FIGURE LEGENDS**

292 **Figure S1. Negative-stain EM images of variants with left-shifted SEC peaks.**

293 **Figure S2. Negative-stain EM images of well-folded particles.**

294 **Figure S3. Characterization of a disulfide and cavity-filling combination variant**
295 **(Combo23).** (A) SEC traces of S-2P, Combo23, and the parental variants S884C/A893C
296 (disulfide bond) and L938F (cavity filling). (B) DSF melting temperature analysis of S-2P,
297 Combo23, and its parental variants. The black dashed line represents the Tm of S-2P, and the
298 purple dashed line represents the Tm of S884C/A893C.

299 **Figure S4. Cryo-EM data processing workflow.**

300 **Figure S5. Cryo-EM structure validation.** FSC curves and viewing distribution plots,
301 generated in cryoSPARC v2.15, are shown for both the two-RBD-up (*left*) and the one-RBD-up
302 (*right*) reconstruction. Cryo-EM density of each reconstruction is shown and colored according
303 to local resolution, with a central slice through the density shown to the right.

304 **Table S1. Expression summary of variants with single substitutions.**

305 **Table S2. Expression summary of Combo variants.**

306 **Table S3. Cryo-EM data collection and refinement statistics.**

307 **METHODS**

308 Design scheme for prefusion-stabilized SARS-CoV-2 spike variants

309 The SARS-CoV-2 S-2P variant was used as the base construct for all subsequent designs²¹. The
310 S-2P base construct comprises residues 1-1208 of SARS-CoV-2 S (GenBank: MN908947) with
311 prolines substituted at residues 986 and 987, “GSAS” substituted at the furin cleavage site
312 (residues 682–685), and C-terminal foldon trimerization motif, HRV3C protease recognition site,
313 Twin-Strep-tag and octa-histidine tag cloned into the mammalian expression plasmid pαH. Using
314 this plasmid as a template, desired mutations were introduced at selected positions within the
315 SARS-CoV-2 S2 subunit. Based on SARS-CoV-2 S-2P cryo-EM structure (PDB ID: 6VSB),
316 pairs of residues with C β atoms less than 4.6 Å apart were considered for disulfide bond designs.
317 We particularly targeted the regions that move drastically during the pre- to postfusion transition
318 such as the fusion peptide, connector region and HR1. Salt bridge variants required that the
319 charged groups of the substituted residues were predicted to be within 4.0 Å. For residues in
320 loops, a slightly longer distance than 4.0 Å was allowed. Core-facing residues with sidechains
321 adjacent to a pre-existing internal cavity were examined for potential substitutions to bulkier
322 hydrophobic residues. Proline substitutions were designed in the FP, connector region, or HR1
323 and placed either in a flexible loop or at the N-terminus of a helix. Combinations were chosen to
324 test whether pairs of the same type of design (e.g. disulfide/disulfide) or different types of
325 designs (e.g. disulfide/proline) could result in additive effects on spike expression and stability.

326 Protein expression and purification

327 Plasmids encoding S variants were transiently transfected into FreeStyle 293-F cells (Thermo
328 Fisher) using polyethyleneimine, with 5 μM kifunensine being added 3h post-transfection.
329 Cultures were harvested four days after transfection and the medium was separated from the cells
330 by centrifugation. Supernatants were passed through a 0.22 μm filter and then over StrepTactin

331 resin (IBA). Spike variants were further purified by size-exclusion chromatography using a
332 Superose 6 10/300 column (GE Healthcare) in a buffer composed of 2 mM Tris pH 8.0, 200 mM
333 NaCl and 0.02% NaN₃. For initial purification and characterization, single-substitution and
334 combination spike variants were purified from 40 mL cultures. For the 2L HexaPro purification,
335 the size-exclusion column used was a Superose 6 16/600 column (GE Healthcare).

336 ExpiCHO cells were transiently transfected with a plasmid encoding HexaPro using
337 Expifectamine, and cells were grown for six days at 32 °C according to the manufacturer's High
338 Titer protocol (Thermo Fisher). Supernatants were then passed through a 0.22 µm filter and
339 batch-purified using IMAC resin (Sigma-Aldrich). The IMAC elution was then purified by size-
340 exclusion chromatography using a Superose 6 10/300 column (GE Healthcare) in a buffer
341 composed of 2 mM Tris pH 8.0, 200 mM NaCl and 0.02% NaN₃.

342 Differential scanning fluorimetry

343 In a 96-well qPCR plate, solutions were prepared with a final concentration of 5X SYPRO
344 Orange Protein Gel Stain (Thermo Fisher) and 0.25 mg/ml spike. Continuous fluorescence
345 measurements ($\lambda_{\text{ex}}=465$ nm, $\lambda_{\text{em}}=580$ nm) were performed using a Roche LightCycler 480 II,
346 using a temperature ramp rate of 4.4 °C/minute increasing from 22 °C to 95 °C. Data were
347 plotted as the derivative of the melting curve as a function of temperature.

348 Negative stain EM

349 Purified SARS-CoV-2 S variants were diluted to a concentration of 0.04 mg/mL in 2 mM Tris
350 pH 8.0, 200 mM NaCl and 0.02% NaN₃. Each protein was deposited on a CF-400-CU grid
351 (Electron Microscopy Sciences) that had been plasma cleaned for 30 seconds in a Solarus 950
352 plasma cleaner (Gatan) with a 4:1 ratio of O₂/H₂ and stained using methylamine tungstate

353 (Nanoprobes). Grids were imaged at a magnification of 92,000X (corresponding to a calibrated
354 pixel size of 1.63 Å/pix) in a Talos F200C TEM microscope equipped with a Ceta 16M detector
355 (Thermo Fisher). Stability experiments with S-2P and HexaPro were performed by imaging
356 samples as described above after 3 rounds of snap freezing with liquid nitrogen and thawing,
357 after storing samples at room temperature for 1-2 days, or after incubating at 50 °C, 55 °C, or 60
358 °C for 30 minutes in a thermal cycler.

359 *Biolayer interferometry for quantification of protein expression*

360 Plasmids encoding spike variants were transfected into FreeStyle 293-F cells (Thermo Fisher) in
361 3 mL of medium and harvested four days after transfection. After centrifugation, supernatant was
362 diluted 5-fold with buffer composed of 10 mM HEPES pH 7.5, 150 mM NaCl, 3 mM EDTA,
363 0.05% Tween 20 and 1 mg/mL bovine serum albumin. Anti-foldon IgG was immobilized to an
364 anti-human Fc (AHC) biosensor (FortéBio) using an Octet RED96e (FortéBio). The IgG loaded
365 biosensor was then dipped into wells containing individual spike variants. A standard curve was
366 determined by measuring 2-fold serial dilutions of purified S-2P at concentrations ranging from
367 10 µg/mL to 0.16 µg/mL. The data were reference-subtracted, aligned to a baseline after IgG
368 capture and quantified based on a linear fit of the initial slope for each association curve using
369 Octet Data Analysis software v11.1.

370 *Surface plasmon resonance*

371 His-tagged HexaPro was immobilized to a NiNTA sensorchip (GE Healthcare) to a level of ~500
372 response units (RUs) using a Biacore X100 (GE Healthcare) and running buffer composed of 10
373 mM HEPES pH 8.0, 150 mM NaCl and 0.05% Tween 20. Serial dilutions of purified hACE2
374 were injected at concentrations ranging from 250 to 15.6 nM. Response curves were fit to a 1:1
375 binding model using Biacore X100 Evaluation Software (GE Healthcare).

376 *Cryo-EM sample preparation and data collection*

377 Purified HexaPro was diluted to a concentration of 0.35 mg/mL in 2 mM Tris pH 8.0, 200 mM
378 NaCl, 0.02% NaN₃ and applied to plasma-cleaned CF-400 1.2/1.3 grids before being blotted for
379 6 seconds in a Vitrobot Mark IV (Thermo Fisher) and plunge frozen into liquid ethane. 3,511
380 micrographs were collected from a single grid using a FEI Titan Krios (Thermo Fisher) equipped
381 with a K3 detector (Gatan). Data were collected at a magnification of 81,000x, corresponding to
382 a calibrated pixel size of 1.08 Å/pix. A full description of the data collection parameters can be
383 found in **Table S3**.

384 *Cryo-EM data processing*

385 Motion correction, CTF-estimation and particle picking were performed in Warp³⁴. Particles
386 were then imported into cryoSPARC v2.15.0 for 2D classification, *ab initio* 3D reconstruction,
387 heterogeneous 3D refinement and non-uniform homogeneous refinement³⁵. The one-RBD-up
388 reconstruction was subjected to local B-factor sharpening using LocalDeBlur³⁶ and the two-
389 RBD-up reconstruction was sharpened in cryoSPARC. Iterative model building and refinement
390 were performed with Coot, Phenix and ISOLDE³⁷⁻³⁹.

REFERENCES

1. Peiris, J. S. M. *et al.* Coronavirus as a possible cause of severe acute respiratory syndrome. *Lancet* **361**, 1319–1325 (2003).
2. Zaki, A. M., Van Boheemen, S., Bestebroer, T. M., Osterhaus, A. D. M. E. & Fouchier, R. A. M. Isolation of a novel coronavirus from a man with pneumonia in Saudi Arabia. *N. Engl. J. Med.* **367**, 1814–1820 (2012).
3. Chan, J. F. W. *et al.* A familial cluster of pneumonia associated with the 2019 novel coronavirus indicating person-to-person transmission: a study of a family cluster. *Lancet* **395**, 514–523 (2020).
4. Huang, C. *et al.* Clinical features of patients infected with 2019 novel coronavirus in Wuhan, China. *Lancet* **395**, 497–506 (2020).
5. Li, F. Structure, Function, and Evolution of Coronavirus Spike Proteins. *Annu. Rev. Virol.* **3**, 237–261 (2016).
6. Siebert, D. N., Bosch, B. J., van der Zee, R., de Haan, C. A. M. & Rottier, P. J. M. The Coronavirus Spike Protein Is a Class I Virus Fusion Protein: Structural and Functional Characterization of the Fusion Core Complex. *J. Virol.* **77**, 8801–8811 (2003).
7. Mille, J. K. & Whittaker, G. R. Host cell entry of Middle East respiratory syndrome coronavirus after two-step, furin-mediated activation of the spike protein. *Proc. Natl. Acad. Sci. U. S. A.* **111**, 15214–15219 (2014).
8. Hoffmann, M. *et al.* SARS-CoV-2 Cell Entry Depends on ACE2 and TMPRSS2 and Is Blocked by a Clinically Proven Protease Inhibitor. *Cell* **181**, 271–280.e8 (2020).

9. Wan, Y., Shang, J., Graham, R., Baric, R. S. & Li, F. Receptor Recognition by the Novel Coronavirus from Wuhan: an Analysis Based on Decade-Long Structural Studies of SARS Coronavirus. *J. Virol.* **94**, 1–9 (2020).
10. Zhou, P. *et al.* A pneumonia outbreak associated with a new coronavirus of probable bat origin. *Nature* **579**, 270–273 (2020).
11. Walls, A. C. *et al.* Tectonic conformational changes of a coronavirus spike glycoprotein promote membrane fusion. *Proc. Natl. Acad. Sci. U. S. A.* **114**, 11157–11162 (2017).
12. Buchholz, U. J. *et al.* Contributions of the structural proteins of severe respiratory syndrome coronavirus to protective immunity. *Proc. Natl. Acad. Sci. U. S. A.* **101**, 9804–9809 (2004).
13. Hofmann, H. *et al.* S Protein of Severe Acute Respiratory Syndrome-Associated Coronavirus Mediates Entry into Hepatoma Cell Lines and Is Targeted by Neutralizing Antibodies in Infected Patients. *J. Virol.* **78**, 6134–6142 (2004).
14. Sanders, R. W. *et al.* A next-generation cleaved, soluble HIV-1 Env trimer, BG505 SOSIP.664 gp140, expresses multiple epitopes for broadly neutralizing but not non-neutralizing antibodies. *PLoS Pathog.* **9**, e1003618 (2013).
15. Pallesen, J. *et al.* Immunogenicity and structures of a rationally designed prefusion MERS-CoV spike antigen. *Proc. Natl. Acad. Sci. U. S. A.* **114**, E7348–E7357 (2017).
16. Crank, M. C. *et al.* A proof of concept for structure-based vaccine design targeting RSV in humans. *Science (80-.).* **365**, 505–509 (2019).
17. Park, Y. J. *et al.* Structures of MERS-CoV spike glycoprotein in complex with sialoside

- attachment receptors. *Nat. Struct. Mol. Biol.* **26**, 1151–1157 (2019).
18. Li, Z. *et al.* The human coronavirus HCoV-229E S-protein structure and receptor binding. *Elife* **8**, 1–22 (2019).
19. Wang, N. *et al.* Structural Definition of a Neutralization-Sensitive Epitope on the MERS-CoV S1-NTD. *Cell Rep.* **28**, 3395–3405.e6 (2019).
20. Walls, A. C. *et al.* Unexpected Receptor Functional Mimicry Elucidates Activation of Coronavirus Fusion. *Cell* **176**, 1026–1039.e15 (2019).
21. Wrapp, D. *et al.* Cryo-EM structure of the 2019-nCoV spike in the prefusion conformation. *Science (80-.).* **367**, 1260–1263 (2020).
22. Walls, A. C. *et al.* Structure, Function, and Antigenicity of the SARS-CoV-2 Spike Glycoprotein. *Cell* **181**, 281–292.e6 (2020).
23. McLellan, J. S. *et al.* Structure-based design of a fusion glycoprotein vaccine for respiratory syncytial virus. *Science* **342**, 592–598 (2013).
24. Rutten, L. *et al.* A Universal Approach to Optimize the Folding and Stability of Prefusion-Closed HIV-1 Envelope Trimers. *Cell Rep.* **23**, 584–595 (2018).
25. Yang, L. *et al.* Structure-Guided Redesign Improves NFL HIV Env Trimer Integrity and Identifies an Inter-Protomer Disulfide Permitting Post-Expression Cleavage. *Front. Immunol.* **9**, 1631 (2018).
26. Joyce, M. G. *et al.* Iterative structure-based improvement of a fusion-glycoprotein vaccine against RSV. *Nat. Struct. Mol. Biol.* **23**, 811–820 (2016).
27. Krarup, A. *et al.* A highly stable prefusion RSV F vaccine derived from structural analysis

- of the fusion mechanism. *Nat. Commun.* **6**, 8143 (2015).
28. Rutten, L. *et al.* Structure-Based Design of Prefusion-Stabilized Filovirus Glycoprotein Trimers. *Cell Rep.* **30**, 4540–4550.e3 (2020).
29. Battles, M. B. *et al.* Structure and immunogenicity of pre-fusion-stabilized human metapneumovirus F glycoprotein. *Nat. Commun.* **8**, 1528 (2017).
30. Qiao, H. *et al.* Specific single or double proline substitutions in the ‘spring-loaded’ coiled-coil region of the influenza hemagglutinin impair or abolish membrane fusion activity. *J. Cell Biol.* **141**, 1335–1347 (1998).
31. Hastie, K. M. *et al.* Structural basis for antibody-mediated neutralization of Lassa virus. *Science (80-.).* **356**, 923–928 (2017).
32. Impagliazzo, A. *et al.* A stable trimeric influenza hemagglutinin stem as a broadly protective immunogen. *Science* **349**, 1301–1306 (2015).
33. Henderson, R. *et al.* Controlling the SARS-CoV-2 Spike Glycoprotein Conformation. *bioRxiv* 2020.05.18.102087 (2020). doi:10.1101/2020.05.18.102087
34. Tegunov, D. & Cramer, P. Real-time cryo-electron microscopy data preprocessing with Warp. *Nat. Methods* **16**, 1146–1152 (2019).
35. Punjani, A., Rubinstein, J. L., Fleet, D. J. & Brubaker, M. A. CryoSPARC: Algorithms for rapid unsupervised cryo-EM structure determination. *Nat. Methods* **14**, 290–296 (2017).
36. Ramírez-Aportela, E. *et al.* Automatic local resolution-based sharpening of cryo-EM maps. *Bioinformatics* **36**, 765–772 (2020).
37. Emsley, P., Lohkamp, B., Scott, W. G. & Cowtan, K. Features and development of Coot.

Acta Crystallogr. D. Biol. Crystallogr. **66**, 486–501 (2010).

38. Liebschner, D. *et al.* Macromolecular structure determination using X-rays, neutrons and electrons: Recent developments in Phenix. *Acta Crystallogr. Sect. D Struct. Biol.* **75**, 861–877 (2019).
39. Croll, T. I. ISOLDE: a physically realistic environment for model building into low-resolution electron-density maps. *Acta Crystallogr. Sect. D, Struct. Biol.* **74**, 519–530 (2018).

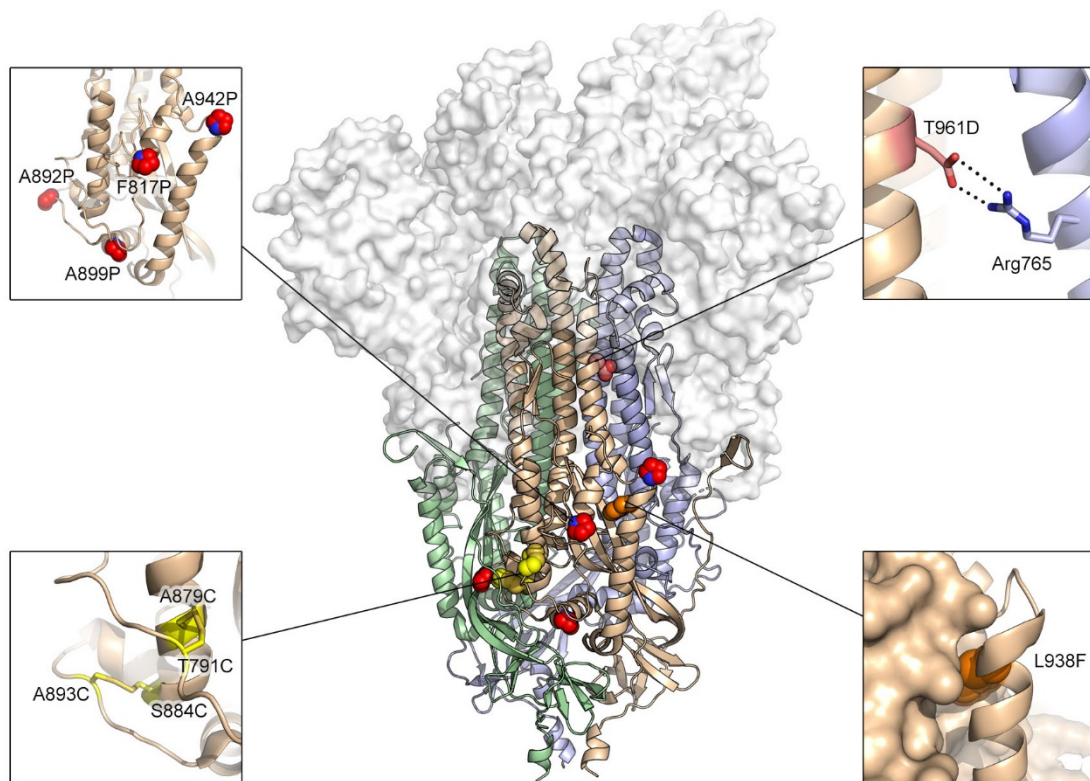


Figure 1. Exemplary substitutions for SARS-CoV-2 spike stabilization. Side view of the trimeric SARS-CoV-2 spike ectodomain in a prefusion conformation (PDB ID: 6VSB). The S1 domains are shown as a transparent molecular surface. The S2 domain for each protomer is shown as a ribbon diagram. Each inset corresponds to one of four types of spike modifications (proline, salt bridge, disulfide, cavity filling). Side chains in each inset are shown as red spheres (proline), yellow sticks (disulfide), red and blue sticks (salt bridge) and orange spheres (cavity filling).

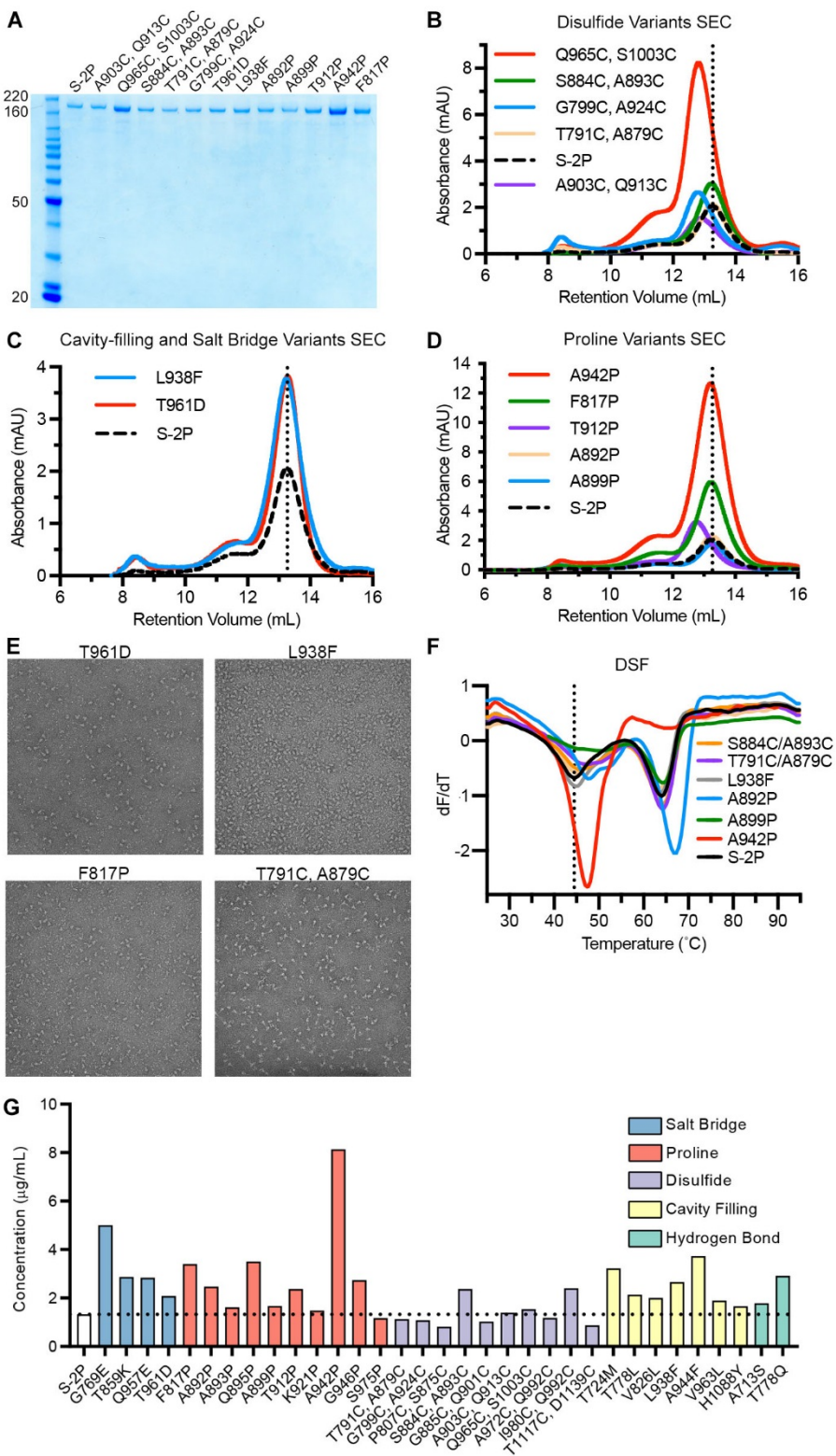


Figure 2. Characterization of single-substitution spike variants. (A) SDS-PAGE of SARS-CoV-2 S-2P and single-substitution spike variants. Molecular weight standards are indicated at the left in kDa. (B-D) Size exclusion chromatography of purified spike variants, grouped by type (B, disulfide variants; C, cavity filling and salt bridge; D, proline). A vertical dotted line indicates the characteristic peak retention volume for S-2P. (E) Representative negative stain electron micrographs for four variants. (F) Differential scanning fluorimetry analysis of spike variant thermostability. The vertical dotted line indicates the first apparent melting temperature for S-2P. (G) Concentrations of individual variants in culture medium, determined by quantitative biolayer interferometry. Variants are colored by type. The horizontal dotted line indicates the calculated concentration of S-2P, which was used as a control for comparison.

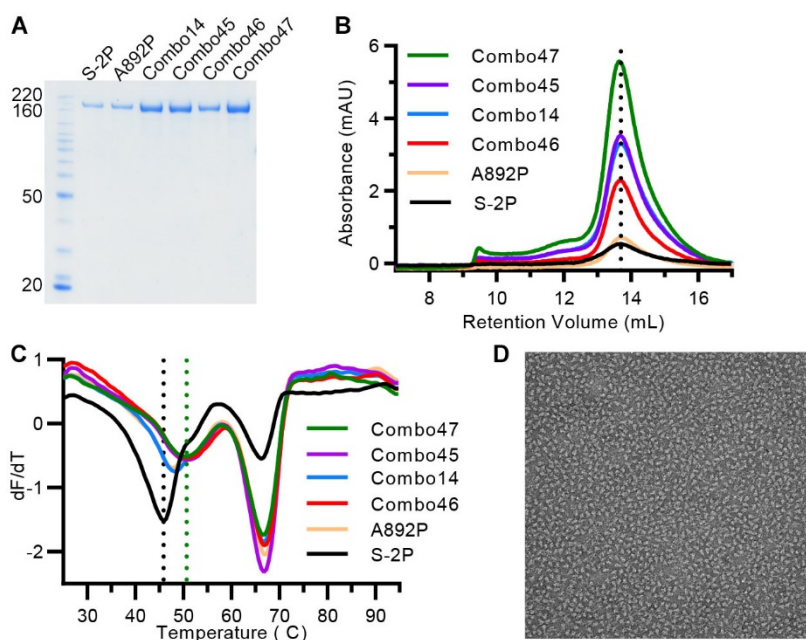


Figure 3. Characterization of multi-substitution spike variants. (A) SDS-PAGE of SARS-CoV-2 Combo variants. Molecular weight standards are indicated at the left in kDa. (B) SEC traces for S-2P, A892P and four Combo variants. The vertical dotted line indicates the peak retention volume for S-2P. (C) DSF analysis of Combo variant thermostability. The black vertical dotted line indicates the first apparent melting temperature for S-2P, the green vertical dotted line shows the first apparent melting temperature for Combo47 (HexaPro). (D) Negative stain electron micrograph of purified Combo47 (HexaPro).

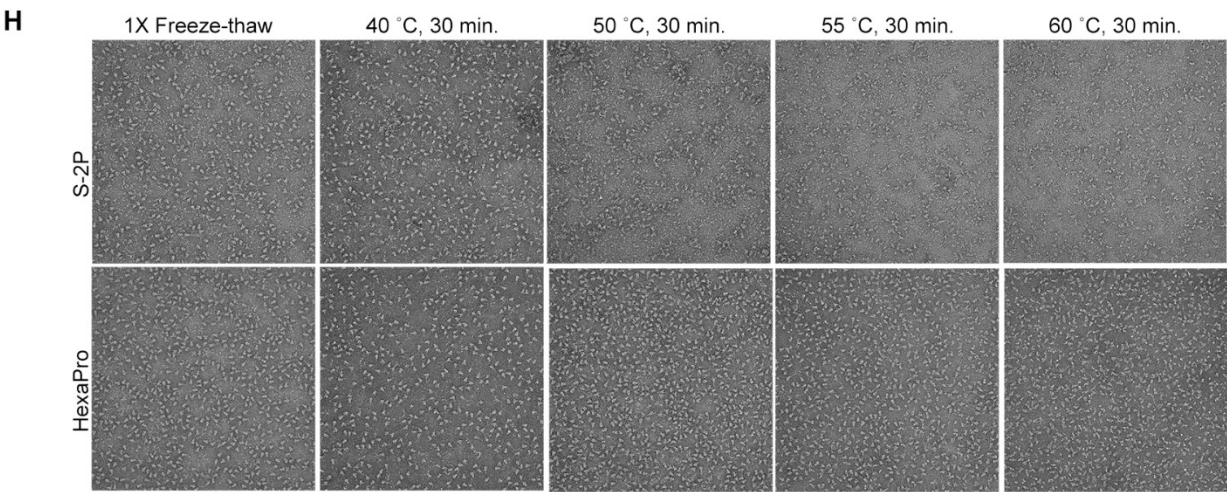
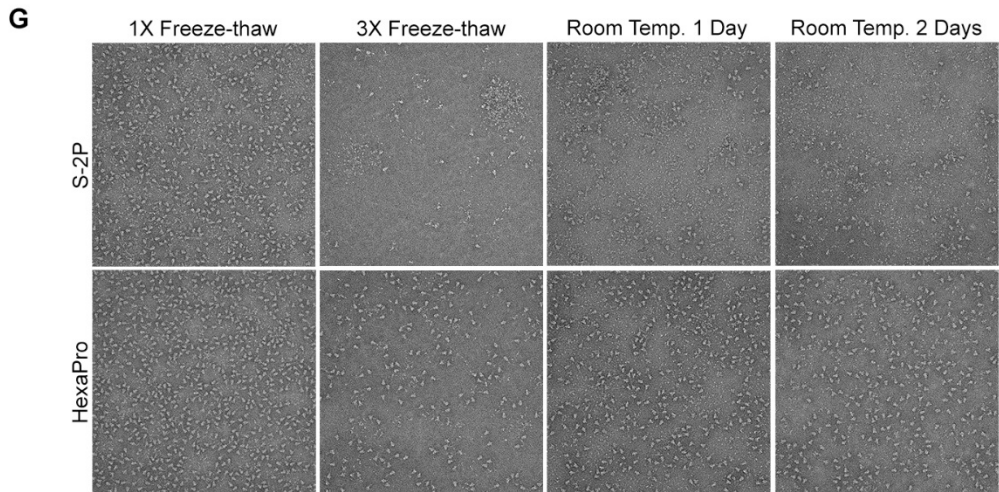
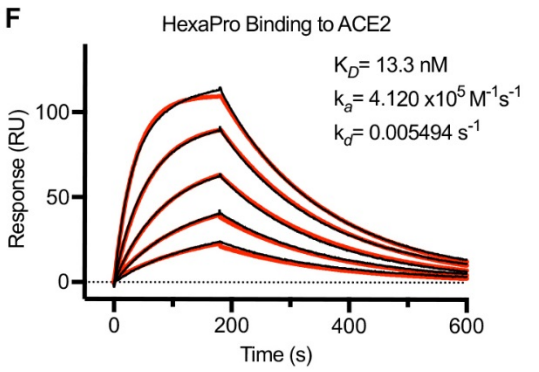
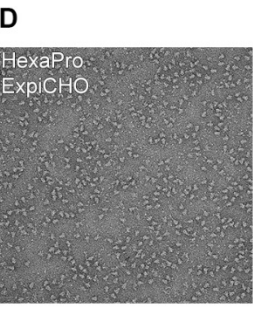
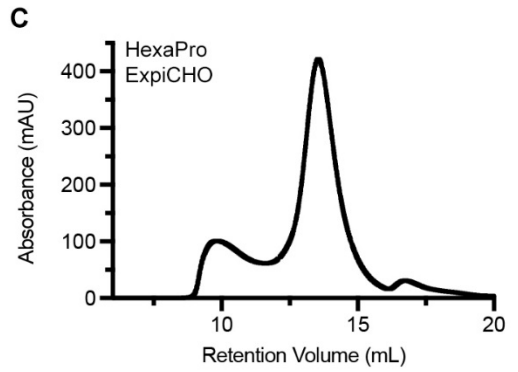
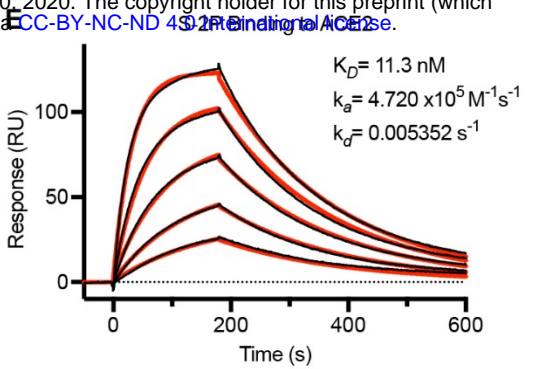
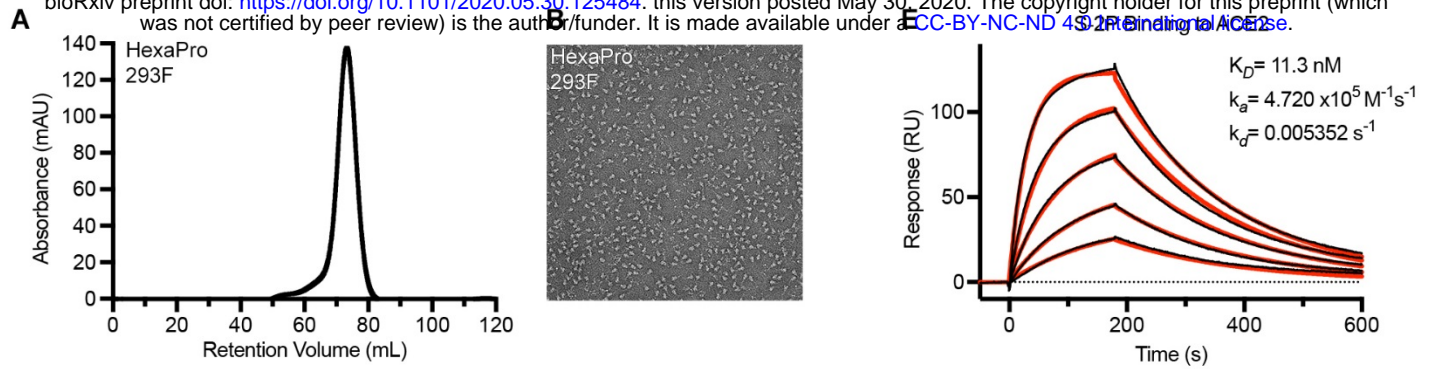


Figure 4. HexaPro exhibits enhanced expression and stability compared to S-2P. (A) SEC trace of a portion of the HexaPro purified from a 2L culture of FreeStyle 293-F cells. (B) Negative stain electron micrograph of HexaPro purified from FreeStyle 293-F cells. (C) SEC trace of HexaPro after purification from a 40 ml culture of ExpiCHO cells. (D) Negative stain electron micrograph of HexaPro purified from ExpiCHO cells. (E-F) Binding of S-2P (E) and HexaPro (F) to human ACE2 assessed by surface plasmon resonance. Binding data are shown as black lines and the best fit to a 1:1 binding model is shown as red lines. (G-H) Assessment of protein stability by negative stain electron microscopy. The top row of micrographs in (G) and (H) corresponds to S-2P, the bottom row corresponds to HexaPro.

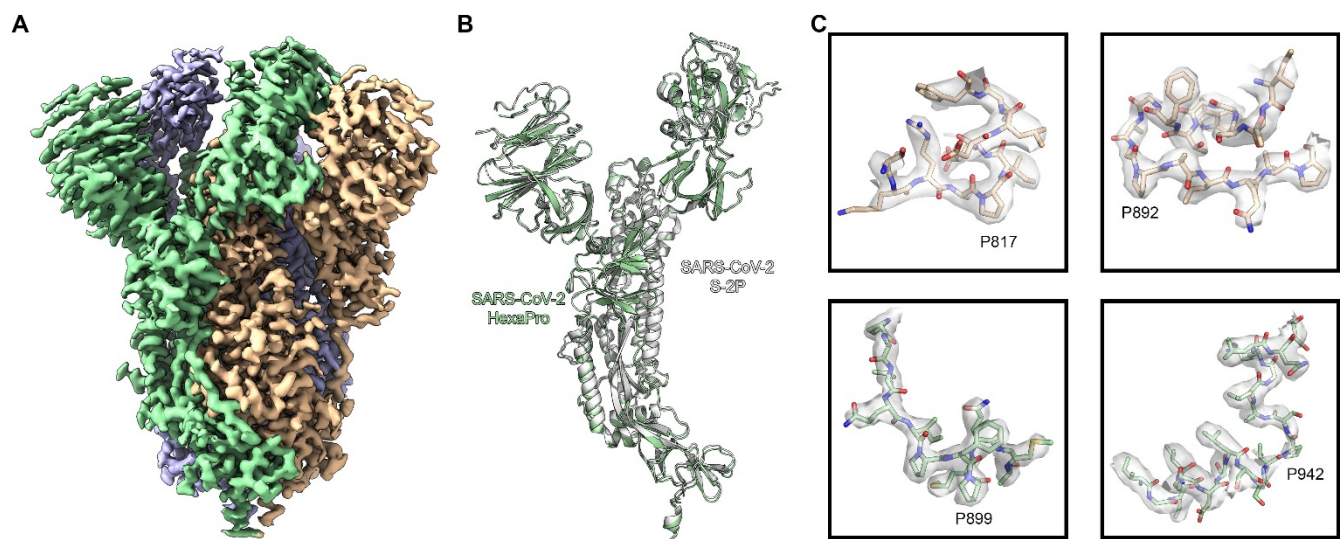


Figure 5. High resolution cryo-EM structure of HexaPro. (A) EM density map of trimeric HexaPro. Each protomer is shown in a different color; the protomer depicted in wheat adopts the RBD-up conformation. (B) Alignment of an RBD-down protomer from HexaPro (green ribbon) with an RBD-down protomer from S-2P (white ribbon, PDB ID: 6VSB). (C) Zoomed view of the four proline substitutions unique to HexaPro. The EM density map is shown as a transparent surface, individual atoms are shown as sticks. Nitrogen atoms are colored blue and oxygen atoms are colored red.

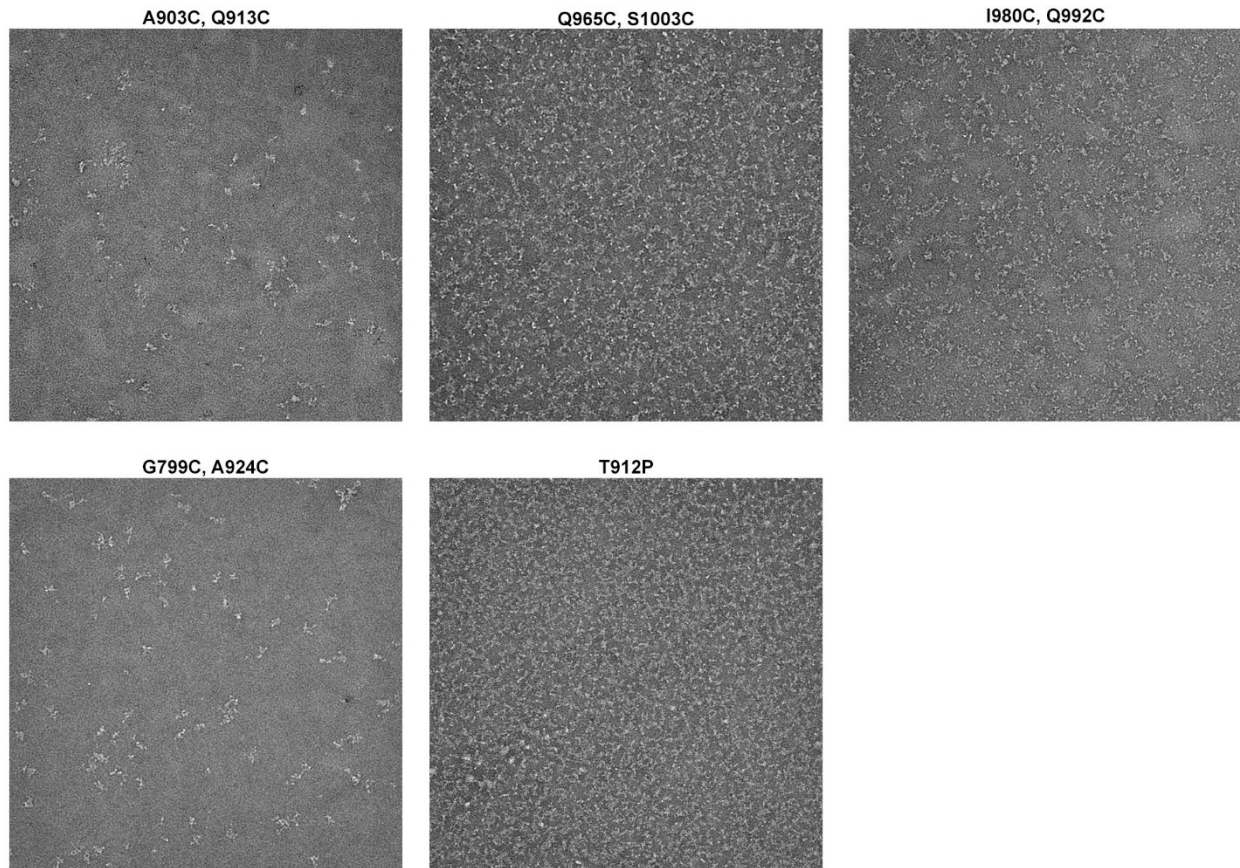


Figure S1. Negative-stain EM images of variants with left-shifted SEC peaks.

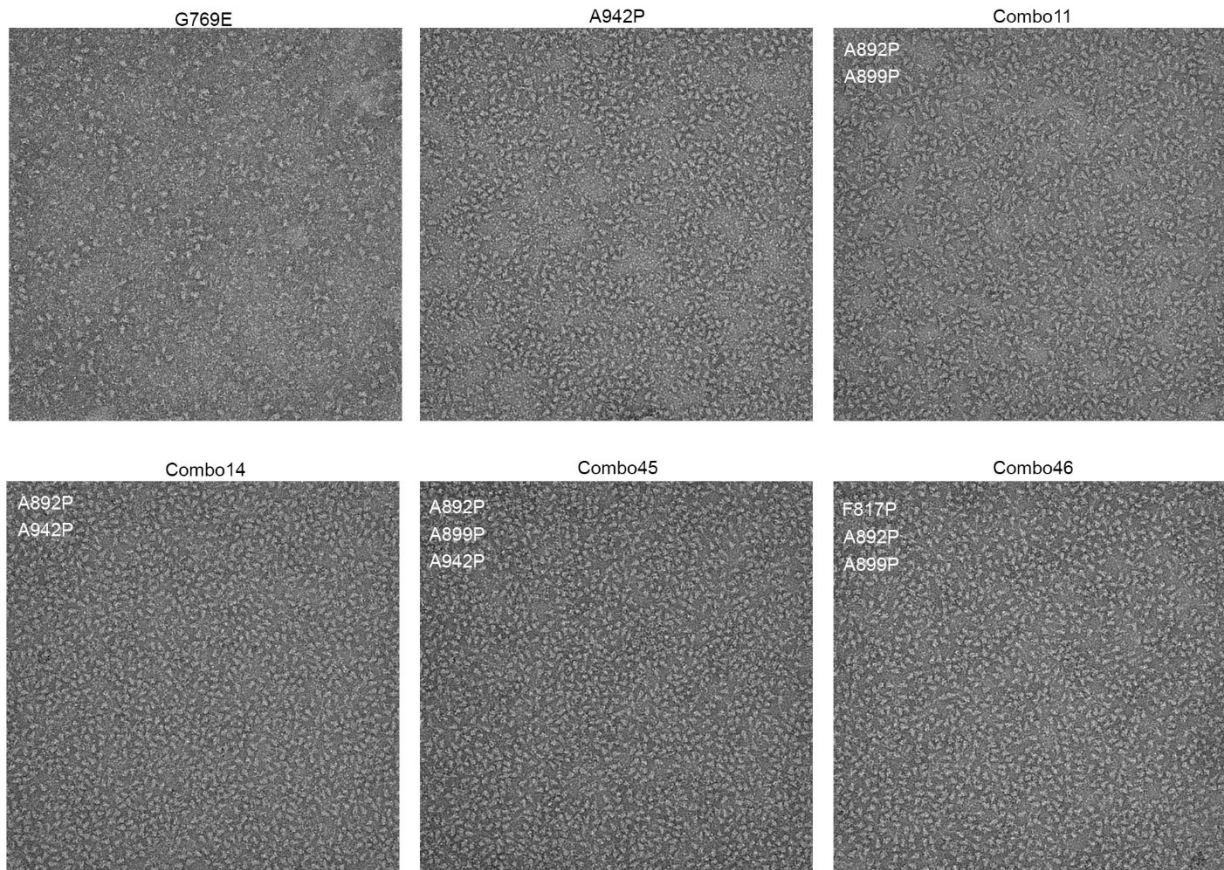


Figure S2. Negative-stain EM images of well-folded particles.

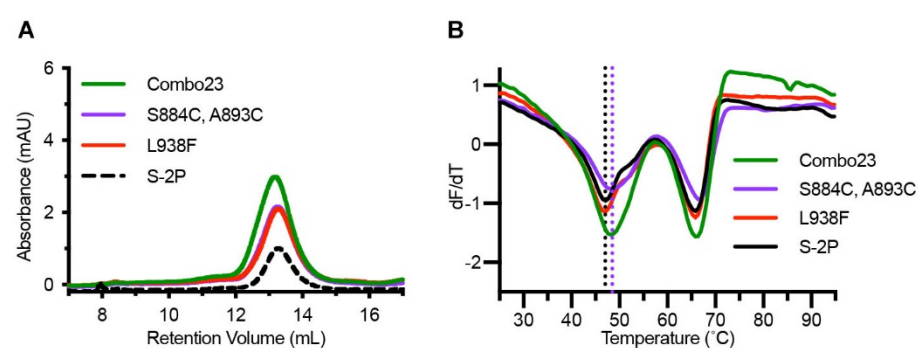


Figure S3. Characterization of a disulfide and cavity-filling combination variant (Combo23). (A) SEC traces of S-2P, Combo23, and the parental variants S884C/A893C (disulfide bond) and L938F (cavity filling). (B) DSF melting temperature analysis of S-2P, Combo23, and its parental variants. The black dashed line represents the T_m of S-2P, and the purple dashed line represents the T_m of S884C/A893C.

Motion Correction
Defocus Estimation
Particle Picking
(Warp)

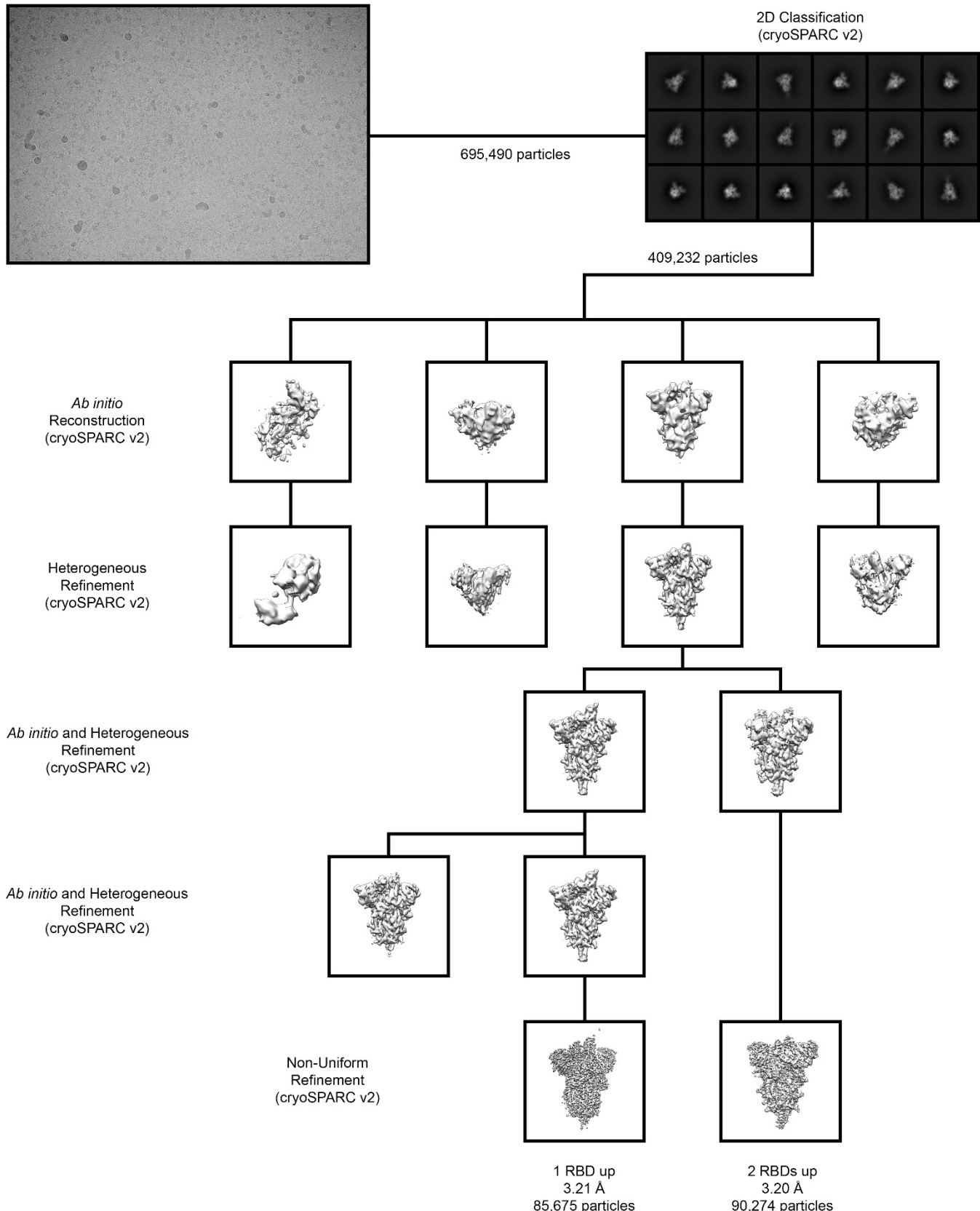


Figure S4. Cryo-EM data processing workflow.

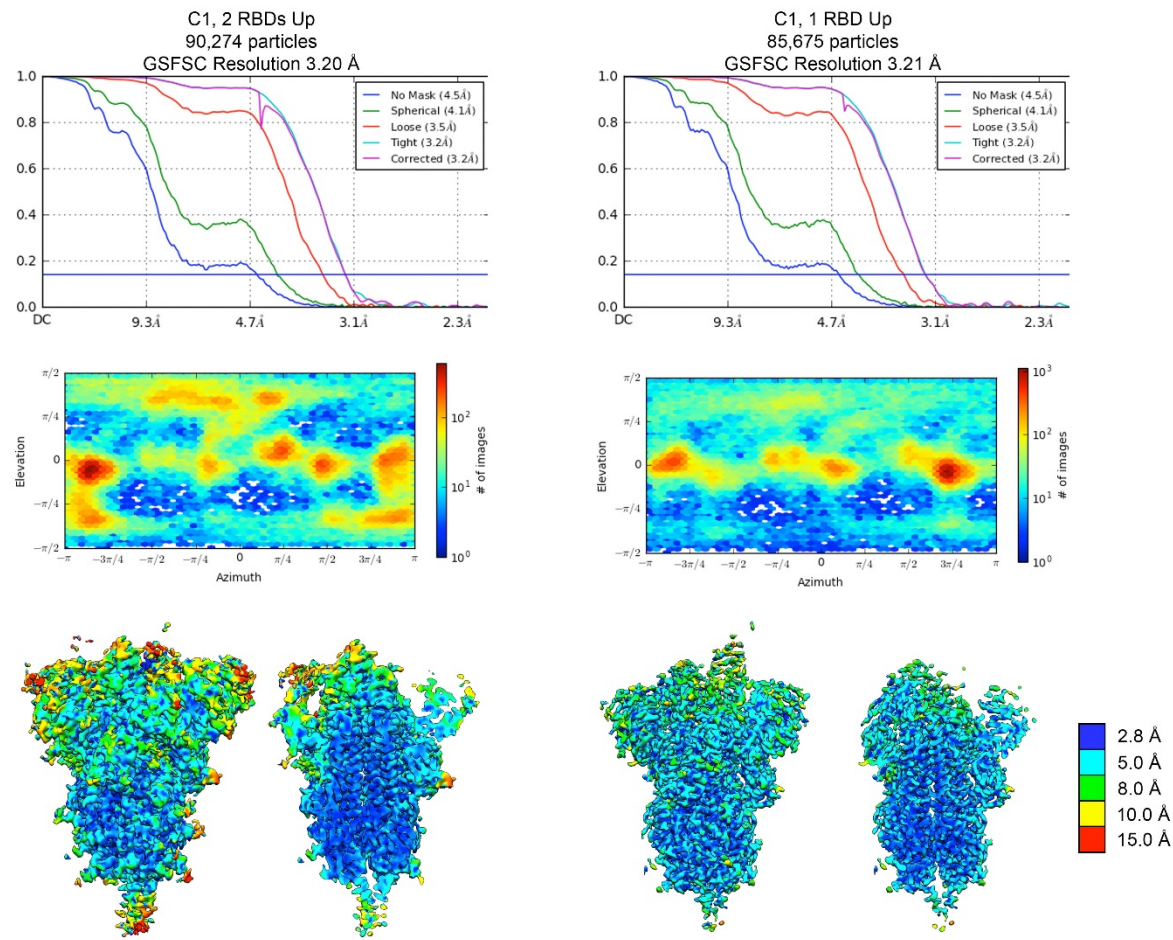


Figure S5. Cryo-EM structure validation. FSC curves and viewing distribution plots, generated in cryoSPARC v2.15, are shown for both the two-RBD-up (*left*) and the one-RBD-up (*right*) reconstruction. Cryo-EM density of each reconstruction is shown and colored according to local resolution, with a central slice through the density shown to the right.

Table S1. Expression summary of variants with single substitutions.

Substitution(s)	Strategy	Fold change in expression relative to S-2P
T547C, N978C	Disulfide	0 ^b
A570C, V963C	Disulfide	0 ^b
S659C, S698C	Disulfide	0.4 ^a
Replace (673-686) with GS	Remove flexible region	0 ^b
Replace (673-686) with GS + A672C, A694C	Disulfide, Remove flexible region	<0.5 ^b
N703Q, V705C, A893C	Disulfide	<0.5 ^b
V705C, A893C	Disulfide	<0.5 ^b
A713S	H bond	1.0 ^a
V722C, A930C	Disulfide	<0.1 ^b
T724M	Cavity-filling	1.3 ^a
L727C, S1021C	Disulfide	<0.5 ^b
P728C, V951C	Disulfide	0 ^b
V729C, A1022C	Disulfide	<0.1 ^a
S730L	Cavity-filling	0 ^b
S730R	Salt bridge	0.15 ^a
S735C, T859C	Disulfide	<0.5 ^b
V736C, L858C	Disulfide	0 ^b
T752K	Salt bridge	<0.5 ^b
A766E	Salt bridge	<0.5 ^b
G769E	Salt bridge	3.0 ^a
I770C, A1015C	Disulfide	<0.5 ^b
T778Q	Hydrogen bond	2.6 ^a
T778L	Cavity-filling	1.5 ^a
T791C, A879C	Disulfide	1.0 ^b
G799C, A924C	Disulfide	1.3 ^a
P807C, S875C	Disulfide	1.1 ^a
F817P	Proline	2.8 ^a
E819C, S1055C	Disulfide	0 ^b
E819C, Q1054C	Disulfide	0 ^b
L822C, A1056C	Disulfide	0 ^b
V826L	Cavity-filling	1.0 ^b
L828K	Salt bridge	0.8 ^a
L828R	Salt bridge	0.4 ^a
Δ(829-851)	Remove flexible region	<0.5 ^b
T859K	Salt bridge	2.1 ^a
P862E	Salt bridge	<0.5 ^b
L865P, Q779M	Proline, cavity-filling	<0.5 ^b
T866P	Proline	<0.5 ^b
I870C, S1055C	Disulfide	0 ^b
T874C, S1055C	Disulfide	<0.5 ^b
S875F	Cavity-filling	<0.5 ^b
S884C, A893C	Disulfide	1.5 ^a
G885C, Q901C	Disulfide	1.1 ^a
G889C, L1034C	Disulfide	<0.1 ^a
A890V	Cavity-filling	1.0 ^b
A892P	Proline, cavity-filling	1.0 ^a
A893P	Proline	1.5 ^b
L894F	Cavity-filling	0.9 ^a
Q895P	Proline	2.1 ^b
I896C, Q901C	Disulfide	0 ^b
A899F	Cavity-filling	0.3 ^b
A899P	Proline, Cav	0.84 ^a
Q901M	Cavity-filling	0.9 ^a
A903C, Q913C	Disulfide	0.82 ^b
V911C, N1108C	Disulfide	0 ^b
T912R	Salt bridge	<0.5 ^b
T912P	Proline cavity-filling	1.5 ^a
K921P	Proline	1.1 ^b
L922P	Proline	0.8 ^b
L938F	Cavity-filling	2.0 ^a
A942P	Proline	6.0 ^a
A944F	Cavity-filling	1.0 ^a
A944F, T724I	Cavity-filling	0.4 ^a
A944Y	Cavity-filling	1.9 ^b
G946P	Proline	1.0 ^b
Q957E	Salt bridge	1.0 ^a
T961D	Salt bridge	1.8 ^a
T961C, S758C	Disulfide	0 ^b
T961C, Q762C	Disulfide	0 ^b
V963L	Cavity-filling	1.8 ^a
Q965C, S1003C	Disulfide	3.8 ^a
A972C, Q992C	Disulfide	1 ^a
A972C, I980C	Disulfide	1.3 ^a

S974C, D979C	Disulfide	0.3 ^b
S975P	Proline	2.2 ^b
N978P	Proline	0.9 ^b
I980C, Q992C	Disulfide	2.0 ^a
R1000Y	Cavity-filling + hydrogen bond	0.3 ^a
R1000W	Cavity-filling	1.0 ^a
S1003V	Cavity-filling	1.9 ^b
I1013F	Cavity-filling	0.8 ^a
R1039F	Charge removal, pi-pi stacking	0.5 ^b
V1040F	Cavity-filling	<0.5 ^b
V1040Y	Cavity-filling	0.3 ^a
H1058W	Cavity-filling	<0.5 ^b
H1058F	Cavity-filling	0 ^b
H1058Y	Cavity-filling	0.3 ^a
A1078C, V1133C	Disulfide	<0.5 ^b
A1080C, I1132C	Disulfide	<0.5 ^b
I1081C, N1135C	Disulfide	0.3 ^a
H1088Y	Cavity-filling	1.6 ^a
H1088W	Cavity-filling	0.6 ^a
F1103C, P1112C	Disulfide	0.15 ^a
V1104I	Cavity-filling	0.7 ^a
T1116C, Y1138C	Disulfide	0 ^b
T1117C, D1139C	Disulfide	1.0 ^a
D1118F	Charge removal, pi-pi stacking	0.5 ^b
I1130Y	Hydrogen bond	0 ^b
L1141F	Cavity-filling	0.8 ^a
ΔHR2 (Δ1161-1208)	Remove flexible region	2.5 ^a

^aQuantified using the area under the curve of the size-exclusion trimer peak

^bQuantified using SDS-PAGE band intensity

Table S2. Expression summary of Combo variants.

Combo #	Substitutions	Strategy	Fold change in expression relative to S-2P
Combo1	A903C, Q913C, Q965C, S1003C	Disulfide+Disulfide	2.2
Combo2	S884C, A893C, A903C, Q913C	Disulfide+Disulfide	0.8
Combo3	T791C, A879C, A903C, Q913C	Disulfide+Disulfide	0.5
Combo4	G799C, A924C, A903C, Q913C	Disulfide+Disulfide	0.5
Combo8	T791C, A879C, S884C, A893C	Disulfide+Disulfide	0.5
Combo9	G799C, A924C, S884C, A893C	Disulfide+Disulfide	0.4
Combo11	A892P, A899P	Proline+Proline	1.9
Combo12	A892P, T912P	Proline+Proline	2.7
Combo14	A892P, A942P	Proline+Proline	6.2
Combo16	A899P, A942P	Proline+Proline	5.1
Combo19	L938F, A892P	Cavity-filling+Proline	3.0
Combo20	L938F, A899P	Cavity-filling+Proline	3.0
Combo21	F817P, L938F	Proline+Proline	3.9
Combo22	L938F, A942P	Cavity-filling+Proline	6.0
Combo23	S884C, A893C, L938F	Disulfide+Cavity-filling	2.9
Combo24	T791C, A879C, L938F	Disulfide+Cavity-filling	2.2
Combo26	L938F, A903C, Q913C	Cavity-filling+Disulfide	2.0
Combo40	F817P, S884C, A893C	Proline+Disulfide	2.0
Combo42	T791C, A879C, F817P	Disulfide+Proline	1.4
Combo45	A892P, A899P, A942P	3X Proline	6.2
Combo46	F817P, A892P, A899P	3X Proline	3.8
Combo47	F817P, A892P, A899P, A942P	4X Proline	9.8

Table S3. Cryo-EM data collection and refinement statistics.

EM data collection and reconstruction statistics

Protein	SARS-CoV-2 S HexaPro One RBD Up	SARS-CoV-2 S HexaPro Two RBDs Up
EMDB		
Microscope	FEI Titan Krios	FEI Titan Krios
Voltage (kV)	300	300
Detector	Gatan K3	Gatan K3
Magnification	81,000	81,000
Pixel size (Å/pix)	1.08	1.08
Frames per exposure	40	40
Exposure (e-/Å ²)	45	45
Defocus range (μm)	0.8-2.3	0.8-2.3
Micrographs collected	2,436	2,436
Particles extracted/final	695,490 / 85,675	695,490 / 90,274
Symmetry imposed	n/a (C1)	n/a (C1)
Masked resolution at 0.143 FSC (Å)	3.21	3.20

Model refinement and validation statistics

PDB	
Composition	
Amino acids	2,920
Glycans	50
RMSD bonds (Å)	0.007
RMSD angles (°)	0.995
Mean B-factors	
Amino acids	37.8
Glycans	55
Ramachandran	
Favored (%)	95.4
Allowed (%)	4.5
Outliers (%)	0.1
Rotamer outliers (%)	3.7
Clash score	6.72
C-beta outliers (%)	0.0
CaBLAM outliers (%)	2.75
MolProbity score	2.12
EMRinger score	2.87